

# Analytical theory for three wave-mixing processes in a slightly deformed cylinder

Raksha Singla\* and W. Luis Mochán†

*Instituto de Ciencias Físicas, Universidad Nacional Autónoma de México,  
Avenida Universidad s/n, 62210 Cuernavaca, Morelos, México*

arXiv:2106.06501v1 [physics.optics] 11 Jun 2021

# Abstract

The second order optical response of centrosymmetric materials manifests itself mostly at their surface, being strongly suppressed in their bulk. However, the overall surface response is also suppressed in nanoparticles with a centrosymmetric geometry subjected to homogeneous fields. Nevertheless, nanoparticles with a *noncentrosymmetric geometry* do exhibit second order optical properties. We develop an analytical theory to investigate the second order optical response of a noncentrosymmetric thin cylinder with a slightly deformed cross-section made up of a centrosymmetric material subjected to two monochromatic fields. We calculate the linear and nonlinear near fields perturbatively using the extent of the deformation away from a circular cross-section as the perturbation parameter. We obtain expressions for the quadratic hyperpolarizabilities in terms of the linear response evaluated at the three frequencies involved. We analyze the spectral features of the nonlinear response functions and explore their resonant structure for a model dielectric cylinder. Furthermore, we evaluate the second order radiated fields, the radiation patterns and efficiency of the different quadratic processes. We obtain a strong competition between electric dipolar, magnetic dipolar and electric quadrupolar contributions even for very small deformations.

## I. INTRODUCTION

Nonlinear optics plays a key role in the development of many modern photonic technologies such as super continuum generation[1], holography[2], optical parametric amplification[3], generation of ultra-short pulses[4, 5], etc. Since optical nonlinear processes are inherently weak, devices made from conventional nonlinear crystals require strong excitation fields and phase matching conditions for them to be efficient. Advances in nanotechnology have led to the development of a plethora of nanomaterials which exhibit remarkable optical nonlinearities with unparalleled applications such as in miniaturization of photonic devices[6, 7]. The nonlinear dependence on the electric field yields an amplification of the response in these novel nanomaterials. The presence of processes that enhance the local field, for example, plasmonic resonances in metallic nanoparticles have been shown to boost the nonlinear efficiency[8, 9]. Recently, all dielectric nanostructures have also been reported with excep-

---

\* [raksharuia@icf.unam.mx](mailto:raksharuia@icf.unam.mx)

† [mochan@icf.unam.mx](mailto:mochan@icf.unam.mx)

tional nonlinear conversion efficiencies[10–12]. Understanding the underlying mechanisms of nonlinear processes and their enhancement in these structures has been a topic of growing interest. Various nonlinear processes such as second harmonic generation (SHG)[13, 14], two photon absorption (TPA)[15], third harmonic generation (THG)[11, 16], and four wave mixing (FWM)[17, 18] have been observed in different nanostructures and their applications have been discussed.

Second order nonlinear processes involve photon-photon interactions assisted by materials that lead to various three-wave mixing effects such as the generation of radiation with the sum (SFG) ( $\omega_+ = \omega_1 + \omega_2$ ) or the difference (DFG) ( $\omega_- = \omega_1 - \omega_2$ ) of the frequencies  $\omega_1$  and  $\omega_2$  of two driving fields, conversion of these input signals to their second harmonics (SHG)  $2\omega_1$  or  $2\omega_2$ , or the generation of a static quadratic polarization, optical rectification (OR). The quadratic susceptibility tensor, originating due to electric-dipolar transitions, is zero within the bulk of a centrosymmetric medium and hence the second order response manifests itself mainly at its surface where the inversion symmetry is locally lost. For this reason, the different second order processes have been extensively used as surface probes for these class of materials[19–22]. Besides providing remarkable non-invasive surface imaging techniques, they have demonstrated tremendous potential for numerous other applications, as in the development of coherent light sources at different frequencies. For example, SFG has been used in the production of light sources in the UV-Vis spectral range[23, 24] and DFG for sources at mid or far infra-red frequencies[25–27]. Generation of the previously inaccessible terahertz (THz) frequency band have also been facilitated by DFG[28, 29].

The selection rules for the second order optical properties of centrosymmetric bulk materials are also applicable to nanoparticles made up of them, with the second order response being generated largely at their surfaces. However, for particles with a centrosymmetric shape, an exact cancellation of the induced quadratic polarization from opposite points of the surface leads to a null overall response. A second order response, may still be observed in such cases, but it is due to multipolar excitations. On the other hand, dipole driven second order response from particles with *noncentrosymmetric geometry* may be observed, as the local contributions from each point of the surface do not cancel. SHG[9, 30, 31] and DFG[32, 33] from noncentrosymmetric nanoparticles or nanostructures have been studied extensively, using both experimental and numerical means.

In a previous work we have developed an analytical theory for the optical SHG of a

noncentrosymmetric cylinder[14]. Here, we present a calculation of the response using an approximate analytical perturbative theory and generalize it to explore all the second order optical processes, namely, SFG, DFG, OR, and the previously discussed SHG, though including in the latter the possibility of excitation by noncollinear fundamental fields. To this end, we choose an isolated long cylinder with a noncentrosymmetric cross-section, as in Ref. [14]. We consider two monochromatic fields with polarizations normal to the axis of the cylinder, and compute the linear and the nonlinear fields induced within and outside the cylinder, generalizing the perturbative approach of Ref. [14]. We employ the *dipolium* model[34] to obtain the nonlinear response within the bulk and on the surface of the cylinder. That model was originally developed to explore the SH response, and was later extended towards the SF response of conductors[35]. Within the dipolium theory, the material is modeled as a homogeneous array of polarizable entities that respond harmonically to the electromagnetic field. The origin of the nonlinearity in the model is the non-homogeneity of the fields, including their abrupt variation across interfaces. For the sake of completeness, we present a brief description of the model and a derivation of the DF nonlinear surface and bulk susceptibilities which we write in terms of some dimensionless parameters[36] that depend on the linear dielectric response evaluated at the frequencies involved. Then we extend our results to get also the SF, SH and OR responses. Furthermore, we calculate the nonlinear fields in the radiation zone and analyze the efficiency of the different second order processes.

The structure of the paper is the following. In Sec. II A, we describe our theory to calculate the generation of a DF signal from a planar surface. In Sec. II B we calculate the DF response of the cylinder, assuming it is locally flat. We find the DF efficiency in Sec. II C and generalize it to the SF, SH and OR cases. Section III illustrates our results for a model dielectric cylinder. Finally, we present our conclusions in Sec. IV.

## II. THEORY

### A. Response of a semi-infinite system

We consider a semi-infinite *dipolium* [34], a homogeneous array of harmonic polarizable entities. Each polarizable entity is represented by an electron of charge  $-e$  and mass  $m$  at a

separation  $\mathbf{x}$  from its equilibrium position  $\mathbf{r}_0$  to which it is bound by a harmonic force with resonant frequency  $\omega_0$ . Its classical equation of motion under the influence of a spatially varying external electromagnetic field is

$$m\ddot{\mathbf{x}} = -m\omega_0^2\mathbf{x} - \frac{m}{\tau}\dot{\mathbf{x}} - e\mathbf{E}(\mathbf{r}, t) - \frac{e}{c}\dot{\mathbf{x}} \times \mathbf{B}(\mathbf{r}, t), \quad (1)$$

where we have included a dissipative term characterized by a lifetime  $\tau$ . We remark that the fields should be evaluated at the actual position  $\mathbf{r} = \mathbf{r}_0 + \mathbf{x}$  of the electron, not at its equilibrium position  $\mathbf{r}_0$ . Assuming the displacement  $\mathbf{x}$  from the equilibrium position to be smaller than the scale of variation in the driving fields, we perform a Taylor expansion

$$\mathbf{E}(\mathbf{r}_0 + \mathbf{x}, t) \approx \mathbf{E}(\mathbf{r}_0, t) + \mathbf{x} \cdot \nabla \mathbf{E}(\mathbf{r}_0, t) + \dots \quad (2)$$

Substituting Eq. (2) in the equation of motion (1), we get

$$m\ddot{\mathbf{x}} = -m\omega_0^2\mathbf{x} - \frac{m}{\tau}\dot{\mathbf{x}} - e\mathbf{E}(\mathbf{r}_0, t) - e\mathbf{x} \cdot \nabla \mathbf{E}(\mathbf{r}_0, t) + e\dot{\mathbf{x}} \times \int_{-\infty}^t dt' \nabla \times \mathbf{E}(\mathbf{r}_0, t') + \dots, \quad (3)$$

where we have written the magnetic field  $\mathbf{B}(\mathbf{r}, t) = -c \int_{-\infty}^t dt' \nabla \times \mathbf{E}(\mathbf{r}, t')$  in terms of the electric field, and we assume the electromagnetic field is switched on adiabatically. Notice that the coefficients of  $\mathbf{x}$  and  $\dot{\mathbf{x}}$  in the last two terms depend on time through the spatial derivatives of the field. Thus, Eq. (3) is the equation of a forced, damped harmonic oscillator whose effective *stiffness* varies in time, making it similar to a parametric oscillator. Hence, even though the harmonic oscillator is considered the paradigmatic linear system, it becomes nonlinear through the spatial variations of the driving fields.

We now drive the system with two electromagnetic waves oscillating at frequencies  $\omega_1$  and  $\omega_2$

$$\mathbf{E}(\mathbf{r}, t) = \mathbf{E}_1(\mathbf{r})e^{-i\omega_1 t} + \mathbf{E}_2(\mathbf{r})e^{-i\omega_2 t} + c.c., \quad (4)$$

where  $\mathbf{E}_1(\mathbf{r})$  and  $\mathbf{E}_2(\mathbf{r})$  are complex amplitudes and *c.c.* stands for the complex conjugate. Since the incident optical fields are usually much smaller than the microscopic atomic fields, we employ a perturbative approach to solve Eq. (3) by expanding the solution in powers of  $\mathbf{E}$ ,

$$\mathbf{x}(t) = \mathbf{x}^{(1)}(t) + \mathbf{x}^{(2)}(t) + \dots \quad (5)$$

The linear solution  $\mathbf{x}^{(1)}(t) = \sum_g \mathbf{x}_g^{(1)} e^{-i\omega_g t} + c.c.$ , with  $g = 1, 2$  is a superposition of two oscillations with amplitudes  $\mathbf{x}_g^{(1)}$  corresponding to the incident frequencies  $\omega_g$  respectively,

each obeying the equation of a forced linear harmonic oscillator

$$-m\omega_g^2 \mathbf{x}_g^{(1)} = -m\omega_0^2 \mathbf{x}_g^{(1)} + im\frac{\omega_g}{\tau} \mathbf{x}_g^{(1)} - e\mathbf{E}_g(\mathbf{r}_0, t), \quad (6)$$

whose solution yields the induced linear dipole moment  $\mathbf{p}_g^{(1)} = -e\mathbf{x}_g^{(1)} = \alpha_g \mathbf{E}_g$  where each  $\alpha_g = \alpha(\omega_g)$  is the linear polarizability

$$\alpha(\omega) = \frac{e^2/m}{\mathcal{D}(\omega)}, \quad (7)$$

evaluated at frequency  $\omega_g$ , and

$$\mathcal{D}(\omega) = \omega_0^2 - \omega^2 - i\omega/\tau. \quad (8)$$

We employ the abbreviated notation  $f_g \equiv f(\omega_g)$  for any function  $f$  dependent on frequency. Now we write the second order contribution to Eq. (3),

$$\begin{aligned} m\ddot{\mathbf{x}}^{(2)}(t) = & -m\omega_0^2 \mathbf{x}^{(2)}(t) - \frac{m}{\tau} \dot{\mathbf{x}}^{(2)}(t) - e\mathbf{x}^{(1)}(t) \cdot \nabla \mathbf{E}(\mathbf{r}_0, t) \\ & + e\dot{\mathbf{x}}^{(1)}(t) \times \int^t dt' \nabla \times \mathbf{E}(\mathbf{r}_0, t'). \end{aligned} \quad (9)$$

Notice that upon substitution of  $\mathbf{x}^{(1)}$ , the driving terms in Eq. (9) become quadratic in  $\mathbf{E}$  with several frequency components: DC, the second harmonic of both incident frequencies  $2\omega_g$ , the sum frequency ( $\omega_+ \equiv \omega_1 + \omega_2$ ), and the difference frequency ( $\omega_- \equiv \omega_1 - \omega_2$ ). The equation corresponding to DF is

$$\begin{aligned} \omega_-^2 \mathbf{x}_-^{(2)} = & \omega_0^2 \mathbf{x}_-^{(2)} - i\frac{\omega_-}{\tau} \mathbf{x}_-^{(2)} + \frac{e}{m} \left( \mathbf{x}_1^{(1)} \cdot \nabla \mathbf{E}_2^* + \mathbf{x}_2^{(1)*} \cdot \nabla \mathbf{E}_1 \right) \\ & + \frac{e}{m} \left[ \left( \frac{\omega_1}{\omega_2} \right) \mathbf{x}_1^{(1)} \times \nabla \times \mathbf{E}_2^* + \left( \frac{\omega_2}{\omega_1} \right) \mathbf{x}_2^{(1)*} \times \nabla \times \mathbf{E}_1 \right], \end{aligned} \quad (10)$$

where the superscript (\*) on any quantity denotes its complex conjugate and the subscript - means the corresponding terms are evaluated at  $\omega_-$ . We solve Eq. (10) to obtain the quadratic DF dipole moment  $\mathbf{p}_-^{(2)} = -e\mathbf{x}_-^{(2)}$ ,

$$\begin{aligned} \mathbf{p}_-^{(2)} = & -\frac{1}{e} \alpha_- \left[ \alpha_1 \left( \mathbf{E}_1 \cdot \nabla \mathbf{E}_2^* + \frac{\omega_1}{\omega_2} \mathbf{E}_1 \times (\nabla \times \mathbf{E}_2^*) \right) \right. \\ & \left. + \alpha_2^* \left( \mathbf{E}_2^* \cdot \nabla \mathbf{E}_1 + \frac{\omega_2}{\omega_1} \mathbf{E}_2^* \times (\nabla \times \mathbf{E}_1) \right) \right]. \end{aligned} \quad (11)$$

There are two other second order moments [35] which contribute to the nonlinear DF response: the electric quadrupole moment and the magnetic dipole moment. For convenience,

we define the quadratic electric quadrupole moment as  $\mathbf{Q}_-^{(2)} = -e\mathbf{x}_1^{(1)}\mathbf{x}_2^{(1)*} - e\mathbf{x}_2^{(1)*}\mathbf{x}_1^{(1)}$ . This differs from the usual definition, which is *traceless* and includes a numerical prefactor of 3. Similarly, the DF magnetic moment is given by  $\boldsymbol{\mu}_-^{(2)} = (-e/2mc)\{\mathbf{x}_1^{(1)} \times m\dot{\mathbf{x}}_2^{(1)*} + \mathbf{x}_2^{(1)*} \times m\dot{\mathbf{x}}_1^{(1)}\}$ . From the linear solution we obtain

$$\mathbf{Q}_-^{(2)} = -\frac{1}{e}\alpha_1\alpha_2^*(\mathbf{E}_1\mathbf{E}_2^* + \mathbf{E}_2^*\mathbf{E}_1). \quad (12)$$

and

$$\boldsymbol{\mu}_-^{(2)} = -\frac{i}{2ce}\alpha_1\alpha_2^*(\omega_1 + \omega_2)(\mathbf{E}_1 \times \mathbf{E}_2^*). \quad (13)$$

We must remark here that although these nonlinear moments have been calculated through a classical model, expressions equivalent to the above are obtained for a quantum harmonic oscillator which interacts with the perturbing electromagnetic field through electric-dipolar, magnetic-dipolar and electric-quadrupolar transitions[37].

We consider now a semi-infinite system made from  $n$  of these polarizable entities per unit volume. We assume the system is translationally invariant along the  $x - y$  plane and that its surface lies at  $z = 0$ , across which  $n(z)$  changes rapidly albeit continuously from its bulk value  $n(z \rightarrow \infty) = n_B$  to its vacuum value  $n(z \rightarrow -\infty) = 0$ . The macroscopic nonlinear polarization induced in the system is

$$\mathbf{P}_{-,src}(z) = n(z)\mathbf{p}_-^{(2)} - \frac{1}{2}\nabla \cdot \left( n(z)\mathbf{Q}_-^{(2)} \right) + \frac{ic}{\omega_-}\nabla \times \left( n(z)\boldsymbol{\mu}_-^{(2)} \right). \quad (14)$$

Note that the above expression has the usual electric dipole moment density and an additional term related the non-homogeneity of the electric quadrupolar moment density[38]. Furthermore, it contains a term related to the curl of the quadratic magnetic moment density. This term is not conventional, but it yields the same induced current  $\mathbf{j}_- = \partial\mathbf{P}_-/\partial t$  and is more convenient than keeping only the first two terms in Eq. (14) and adding a nonlinear magnetization[39] and the corresponding magnetization current. The nonlinear polarization (14) is a nonlinear source oscillating at the difference frequency, and it generates an oscillating DF field  $\mathbf{E}_-$ . The linear response of the system to this DF field yields an additional DF polarization, so that substituting Eqs. (11) to (13) into Eq. (14) we get the screened

self-consistent nonlinear polarization

$$\begin{aligned}
\mathbf{P}_-(z) = & n(z)\alpha_- \mathbf{E}_- - \frac{n(z)}{e}\alpha_- \left[ \alpha_1 \left( \mathbf{E}_1 \cdot \nabla \mathbf{E}_2^* + \frac{\omega_1}{\omega_2} \mathbf{E}_1 \times (\nabla \times \mathbf{E}_2^*) \right) \right. \\
& \left. + \alpha_2^* \left( \mathbf{E}_2^* \cdot \nabla \mathbf{E}_1 + \frac{\omega_2}{\omega_1} \mathbf{E}_2^* \times (\nabla \times \mathbf{E}_1) \right) \right] \\
& + \frac{1}{2e}\alpha_1\alpha_2^* \nabla \cdot n(z) (\mathbf{E}_1 \mathbf{E}_2^* + \mathbf{E}_2^* \mathbf{E}_1) \\
& + \frac{1}{2e}\alpha_1\alpha_2^* \left( \frac{\omega_1 + \omega_2}{\omega_-} \right) \nabla (\times n(z) (\mathbf{E}_1 \times \mathbf{E}_2^*)). \tag{15}
\end{aligned}$$

In order to find the *surface response* of the medium, we will only be interested in the thin *selvedge* region whose thickness we can assume is much smaller than the wavelength, allowing us to safely ignore within it the effects of retardation. Thus, we identify  $\mathbf{E}_-$  with the depolarization field

$$E_{-,i} = -4\pi P_{-,z} \delta_{iz}, \tag{16}$$

we drop the  $\nabla \times \mathbf{E}_g$  terms and we ignore the relatively slow spatial variations of the field along the surface. The surface polarization can be obtained after solving Eq. (15) for  $\mathbf{P}_-$  and integrating it across the selvedge,

$$\mathbf{P}_-^s = \int_{\text{se}} dz \mathbf{P}_-(z), \tag{17}$$

where se denotes the selvedge. We define the components of the DF quadratic surface susceptibility tensor through

$$P_{-,i}^s = \sum_{jk} [\chi_{ijk}^s(\omega_1, \bar{\omega}_2) + \chi_{ikj}^s(\bar{\omega}_2, \omega_1)] F_{1,j} F_{2,k}^*, \tag{18}$$

where  $i, j, k$  denote Cartesian components and  $\bar{\omega}_2$  denotes  $-\omega_2$ . Here,  $\mathbf{F}_g = (E_{g,x}, E_{g,y}, D_{g,z})$  is a field whose components are the corresponding components of either  $\mathbf{D}_g$  or  $\mathbf{E}_g$  that are continuous across the surface. We use  $\mathbf{F}_g$  to avoid the ambiguity about the position in the selvedge where the fields are to be calculated. Note that  $j$  and  $k$  are dummy indices and thus can be interchanged. Thus, we may impose the intrinsic permutation symmetry  $\chi_{ijk}^s(\omega_1, \bar{\omega}_2) = \chi_{ikj}^s(\bar{\omega}_2, \omega_1)$ .

From Eqs. (15) and (16) we obtain the normal component of the macroscopic polarization



in the selvedge region,

$$P_{-,z}(z) = \frac{1}{e\epsilon_-(z)} \left[ -n(z)\alpha_- \left( \alpha_1 \frac{1}{\epsilon_1(z)} \frac{\partial}{\partial z} \frac{1}{\epsilon_2^*(z)} + \alpha_2^* \frac{1}{\epsilon_2^*(z)} \frac{\partial}{\partial z} \frac{1}{\epsilon_1(z)} \right) + \alpha_1 \alpha_2^* \frac{\partial}{\partial z} n(z) \frac{1}{\epsilon_1(z)} \frac{1}{\epsilon_2^*(z)} \right] D_{1,z} D_{2,z}^* + 1 \leftrightarrow 2, \quad (19)$$

where we introduced the permittivity

$$\epsilon_g(z) = 1 + 4\pi n(z)\alpha_g, \quad (20)$$

used  $E_{g,z}(z) = D_{g,z}/\epsilon_g(z)$  and assumed  $D_{g,z}$  is constant across the selvedge for  $g = 1, 2, -$ .

The resulting normal component of the DF polarization depends on  $z$  through the density profile  $n(z)$  and its spatial derivatives and is large only within the thin selvedge region where the linear response has a large gradient, and in our long wavelength approximation it vanishes in the bulk and in vacuum. We now integrate Eq. (19) by substituting it in Eq. (17). The integral to be evaluated is of the form  $\int dz f(n(z)) dg(n(z))/dz$ , where  $f$  and  $g$  are rational functions of  $n(z)$ . The integration can be divided into different intervals where  $n$  varies monotonically, which allows us to change integration variable  $z \rightarrow n$ . As the integrands are rational functions of  $n$ , they may be integrated analytically for any density profile  $n(z)$  to obtain the normal component of the nonlinear surface polarization

$$P_{-,z}^s = \chi_{zzz}^s(\omega_1, \bar{\omega}_2) D_{1,z} D_{2,z}^* + 1 \leftrightarrow 2, \quad (21)$$

where

$$\chi_{zzz}^s(\omega_1, \bar{\omega}_2) = -\frac{a(\omega_1, \bar{\omega}_2)}{64\pi^2 n_{BE}} \left( \frac{\epsilon_1 - 1}{\epsilon_1} \right) \left( \frac{\epsilon_2^* - 1}{\epsilon_2^*} \right), \quad (22)$$

and

$$a(\omega_1, \bar{\omega}_2) = -2 \left[ 1 + \frac{(1 - \epsilon_-) \epsilon_1 \epsilon_2^* (\epsilon_2^* \log(\epsilon_-/\epsilon_1) + \text{c.p.})}{(\epsilon_1 - \epsilon_2^*) (\epsilon_2^* - \epsilon_-) (\epsilon_- - \epsilon_1)} \right] \quad (23)$$

is a dimensionless quantity that parameterizes the normal component of the nonlinear surface polarization[36]. Here, c.p. denotes the terms obtained from the previous one through cyclic permutations of the three indices 1, 2, -.

In Fig. 1 we illustrate the behavior of the real and imaginary parts of  $a(\omega_1, \bar{\omega}_2)$  for a model harmonic solid whose dielectric function[40]

$$\epsilon_d(\omega) = \frac{\omega_L^2 - \omega^2 - i\omega/\tau}{\omega_T^2 - \omega^2 - i\omega/\tau} \quad (24)$$

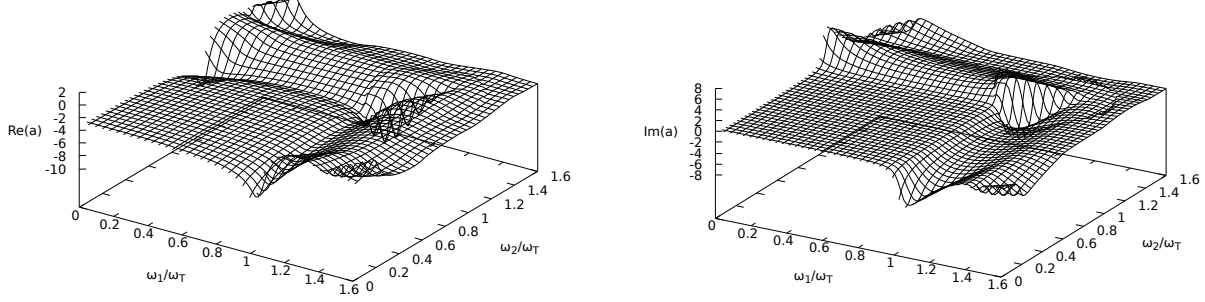


FIG. 1. Real (left panel) and imaginary (right panel) part of  $a(\omega_1, \bar{\omega}_2)$  for a harmonic solid (Eq. (24)) with  $\omega_L = \sqrt{2}\omega_T$  and  $\tau = 20/\omega_T$ , as function of  $\omega_1$  and  $\omega_2$ .

has a single Lorentzian resonance, where  $\omega_L$  and  $\omega_T$  are the frequencies of the longitudinal and transverse optical modes respectively and we included a small dissipation characterized by  $\tau$ . We choose  $\omega_L^2 = 2\omega_T^2$  and  $\tau = 20/\omega_T$ . Between its pole at  $\omega_T$  and its zero at  $\omega_L$ , the dielectric function is negative and the logarithm in Eq. (23) becomes large. Hence, we expect the real and imaginary part of  $a$  to exhibit spectral features in this region. Fig. 1 shows peaks and valleys for both the real and imaginary parts of  $a$  whenever  $\omega_1$  or  $\omega_2$  falls in this region. Moreover, a broad valley along the diagonal  $\omega_1 \approx \omega_2$  is observed in the region where both input frequencies lie in this region, with their difference frequency close to zero. The parameter  $a$  has a constant value for low frequencies and reaches its asymptotic value [41] of  $-2$  for high frequencies.

We follow a similar procedure to that shown above for the parallel component of the nonlinear polarization. Using Eq. (15), we find

$$\begin{aligned} \mathbf{P}_{-,||}(z) = \frac{1}{2e} \alpha_1 \alpha_2^* \left[ \mathbf{E}_{1,||} \frac{\partial n(z)}{\partial z \epsilon_2^*(z)} D_{2,z}^* + \mathbf{E}_{2,||}^* \frac{\partial n(z)}{\partial z \epsilon_1(z)} D_{1,z} \right. \\ \left. + \left( \frac{\omega_1 + \omega_2}{\omega_-} \right) \left( \frac{\partial n(z)}{\partial z \epsilon_2^*(z)} D_{2,z}^* \mathbf{E}_{1,||} - \frac{\partial n(z)}{\partial z \epsilon_1(z)} D_{1,z} \mathbf{E}_{2,||}^* \right) \right], \quad (25) \end{aligned}$$

which we integrate across the selvedge to obtain the nonlinear tangential surface polarization

$$\begin{aligned} \mathbf{P}_{-,||}^s &= \int_{-\infty}^{\infty} dz \mathbf{P}_{-,||}(z) \\ &= \frac{1}{2e} \alpha_1 \alpha_2^* \left[ \frac{n_B}{\epsilon_2^*} \left( 1 + \frac{\omega_1 + \omega_2}{\omega_-} \right) \mathbf{E}_{1,||} D_{2,z}^* + \frac{n_B}{\epsilon_1} \left( 1 - \frac{\omega_1 + \omega_2}{\omega_-} \right) D_{1,z} \mathbf{E}_{2,||}^* \right] \\ &= \chi_{||z}^s(\omega_1, \bar{\omega}_2) \mathbf{E}_{1,||} D_{2,z}^* + \chi_{||z}^s(\omega_1, \bar{\omega}_2) D_{1,z} \mathbf{E}_{2,||}^* + 1 \leftrightarrow 2, \quad (26) \end{aligned}$$

where the surface susceptibility is parameterized as

$$\chi_{\parallel z}^s(\omega_1, \bar{\omega}_2) = \chi_{\parallel z}^s(\bar{\omega}_2, \omega_1) = -\frac{1}{32\pi^2 n_B e} \frac{(\epsilon_1 - 1)(\epsilon_2^* - 1)}{\epsilon_2^*} \frac{\omega_1}{\omega_-} b(\omega_1, \bar{\omega}_2), \quad (27)$$

$$\chi_{\parallel z}^s(\bar{\omega}_2, \omega_1) = \chi_{\parallel z}^s(\omega_1, \bar{\omega}_2) = \frac{1}{32\pi^2 n_B e} \frac{(\epsilon_1 - 1)(\epsilon_2^* - 1)}{\epsilon_1} \frac{\omega_2}{\omega_-} b(\bar{\omega}_2, \omega_1), \quad (28)$$

with

$$b(\omega_1, \bar{\omega}_2) = b(\bar{\omega}_2, \omega_1) = -1. \quad (29)$$

There is another component  $\chi_{z\parallel}^s$  of the surface susceptibility tensor allowed by the in-plane isotropy of the surface[36], but it is null within our model.

We now focus on the bulk quadratic polarization of the system, which we find by substituting Eqs. (11) to (13) in Eq. (14),

$$\mathbf{P}_{-,src}^B = D_1 \mathbf{E}_2^* \cdot (\nabla \mathbf{E}_1) + \tilde{D}_1 (\mathbf{E}_2^* \cdot \nabla) \mathbf{E}_1 + 1 \leftrightarrow 2, \quad (30)$$

where

$$D_g = \frac{1}{16\pi^2 n_B e} (\epsilon_2^* - 1)(\epsilon_1 - 1) \delta_g d_g, \quad (31)$$

$$\tilde{D}_g = \frac{1}{16\pi^2 n_B e} (\epsilon_2^* - 1)(\epsilon_1 - 1) \tilde{\delta}_g \tilde{d}_g, \quad (32)$$

with

$$\delta_1 = -\left(\frac{\epsilon_- - 1}{\epsilon_1 - 1}\right) \frac{\omega_2}{\omega_1}, \quad (33)$$

$$\tilde{\delta}_1 = \frac{\omega_1}{\omega_-} - \left(\frac{\epsilon_- - 1}{\epsilon_1 - 1}\right) \frac{\omega_-}{\omega_1}, \quad (34)$$

$$\delta_2 = -\left(\frac{\epsilon_- - 1}{\epsilon_2^* - 1}\right) \frac{\omega_1}{\omega_2}, \quad (35)$$

$$\tilde{\delta}_2 = -\frac{\omega_2}{\omega_-} + \left(\frac{\epsilon_- - 1}{\epsilon_2^* - 1}\right) \frac{\omega_-}{\omega_2}, \quad (36)$$

and  $d_1 = d_2 = \tilde{d}_1 = \tilde{d}_2 = 1$ . Note that  $P_{-,src}^B$  plays the role of an external source for the DF field in the bulk. The total bulk polarization contains also the polarization linearly induced in response to the self-consistent DF field, as shown in Eq. (15). To obtain the self-consistent DF field Maxwell's equations with sources should be solved with appropriate boundary conditions.

In the dipolium model we assumed all entities to be identical to each other, so it doesn't account for effects such as those arising from the surface electronic structure. We must remark that in a real system these additional effects may not be negligible and must be accounted for in more realistic models. Here, we only focused on the effect of the spatial variation of the field on the second order response.

By construction, the dipolium model above corresponds to a dielectric material. However, it may be shown that its results are equivalent to those of the local jellium model[35], so they may be applied to metals simply by substituting their corresponding dielectric functions. We recall that the results of the dipolium model are valid even for a quantum harmonic oscillator interacting with a perturbing electromagnetic field through electric dipole, electric quadrupole, and magnetic dipole transitions[37].

## B. Response of an isolated nanocylinder

We will now consider an isolated, long cylinder with a noncentrosymmetric geometry but made up of a centrosymmetric material with a nanometric radius. We assume translational symmetry along the axis of the cylinder ( $\hat{z}$  direction), disregarding edge effects as if the cylinder were infinitely long, allowing us to perform all calculations in  $2D$ . We consider a cross-section slightly deformed away from a symmetric circle, described in polar coordinates by

$$r_s(\theta) = r_0(1 + \xi \cos 3\theta), \quad (37)$$

where  $r_0$  is the radius of the nominal cylinder and  $\xi$  characterizes the extent of deformation. This is the most simple noncentrosymmetric deformation of a circle, consisting of three lobes an angle of  $2\pi/3$  apart. The SH for this shape was studied in Ref. [14].

We first excite the system with two monochromatic fields oscillating at frequencies  $\omega_1$  and  $\omega_2$  with polarization on the plane of the cross-section and perpendicular to each other,

$$\mathbf{E}^{\text{ext}}(t) = E_1 e^{-i\omega_1 t} \hat{\mathbf{x}} + E_2 e^{-i\omega_2 t} \hat{\mathbf{y}} + c.c., \quad (38)$$

where  $E_1$  and  $E_2$  are complex amplitudes and we take the corresponding polarization along  $\hat{\mathbf{x}}$  and  $\hat{\mathbf{y}}$  respectively. We disregard the spatial dependence of the fields to concentrate on the effects of the noncentrosymmetric geometry, which is consistent with a long wavelength approximation  $r_0 \ll \lambda_g$  where  $\lambda_g$  ( $g = 1, 2$ ) are the wavelengths of the

incoming waves. We follow the perturbative approach introduced in Ref. [14] to evaluate the self-consistent induced near fields. We start with the general nonretarded solution  $\phi_g(r, \theta) = \phi_g^{\text{in}}(r, \theta)\Theta(r_s(\theta) - r) + \phi_g^{\text{out}}(r, \theta)\Theta(r - r_s(\theta))$  in polar coordinates  $(r, \theta)$  of Laplace's equation for the scalar potential within the particle and in its neighborhood,

$$\phi_g^{\text{in}}(r, \theta) = \sum_{l=0}^{\infty} r^l (s_{gl} \cos l\theta + t_{gl} \sin l\theta), \quad (39a)$$

$$\phi_g^{\text{out}}(r, \theta) = \phi_g^{\text{ex}} + \sum_{l=0}^{\infty} r^{-l} (u_{gl} \cos l\theta + v_{gl} \sin l\theta), \quad (39b)$$

where  $\phi_1^{\text{ex}}(r, \theta) = -E_1 r \cos \theta$ ,  $\phi_2^{\text{ex}}(r, \theta) = -E_2 r \sin \theta$  and  $\Theta$  is the unit step function. We expand the multipolar coefficients  $\zeta_{gl}$  (any of  $s_{gl}$ ,  $t_{gl}$ ,  $u_{gl}$  or  $v_{gl}$ ) as power series on the deformation parameter  $\xi$ ,  $\zeta_{gl} = \sum_{n=0}^{\infty} \zeta_{gl}^{(n)} \xi^n$ . As mentioned previously, we restrict ourselves to small deformations, and we consider terms up to linear order in  $\xi$  only. Using Eqs. (39) and imposing boundary conditions [38] at the interface  $r = r_s(\theta)$ , we obtain the self-consistent linear potential,

$$\frac{\phi_1^{\text{out}}}{E_1} = -r \cos \theta - \frac{1 - \epsilon_1}{1 + \epsilon_1} \frac{r_0^2}{r} \cos \theta + \xi \left[ \left( \frac{1 - \epsilon_1}{1 + \epsilon_1} \right)^2 \frac{r_0^3}{r^2} \cos 2\theta - \frac{1 - \epsilon_1}{1 + \epsilon_1} \frac{r_0^5}{r^4} \cos 4\theta \right], \quad (40a)$$

$$\frac{\phi_1^{\text{in}}}{E_1} = -\frac{2}{1 + \epsilon_1} r \cos \theta + 2\xi \frac{1 - \epsilon_1}{(1 + \epsilon_1)^2} \frac{r^2}{r_0} \cos 2\theta, \quad (40b)$$

$$\frac{\phi_2^{\text{out}}}{E_2} = -r \sin \theta - \frac{1 - \epsilon_2}{1 + \epsilon_2} \frac{r_0^2}{r} \sin \theta - \xi \left[ \left( \frac{1 - \epsilon_2}{1 + \epsilon_2} \right)^2 \frac{r_0^3}{r^2} \sin 2\theta + \frac{1 - \epsilon_2}{1 + \epsilon_2} \frac{r_0^5}{r^4} \sin 4\theta \right], \quad (40c)$$

$$\frac{\phi_2^{\text{in}}}{E_2} = -\frac{2}{1 + \epsilon_2} r \sin \theta - 2\xi \frac{1 - \epsilon_2}{(1 + \epsilon_2)^2} \frac{r^2}{r_0} \sin 2\theta. \quad (40d)$$

The spatial variations of the self-consistent linear fields  $\mathbf{E}_g = -\nabla\phi_g$ , induce a macroscopic nonlinear polarization within the bulk of the cylinder given by Eq. (14) but with a position independent density  $n = n_B$ ,

$$\begin{aligned} \mathbf{P}_{-, \text{src}} = & \frac{E_1 E_2^* \xi}{2\pi^2 n \epsilon r_0} \frac{(1 - \epsilon_1)(1 - \epsilon_2^*)}{(1 + \epsilon_1)^2 (1 + \epsilon_2^*)^2} \left[ - (1 - \epsilon_-)(2 + \epsilon_1 + \epsilon_2^*) + (1 - \epsilon_1 \epsilon_2^*) \right. \\ & \left. + \left( \frac{\omega_1 + \omega_2}{\omega_-} \right) (\epsilon_2^* - \epsilon_1) \right] \left\{ \sin \theta \hat{r} + \cos \theta \hat{\theta} \right\}. \end{aligned} \quad (41)$$

The nonlinear bulk polarization induces a null charge density within the cylinder,

$$\rho_{-, \text{src}} = -\nabla \cdot \mathbf{P}_{-, \text{src}} = 0, \quad (42)$$

up to linear order in the deformation parameter  $\xi$ . The termination of the bulk polarization at the surface of the cylinder induces a *bulk originated* surface nonlinear charge,  $\sigma_{-,src}^b = \mathbf{P}_{-,src} \cdot \hat{\mathbf{n}}$  where  $\hat{\mathbf{n}} = \hat{\mathbf{r}} + 3\xi \sin 3\theta \hat{\boldsymbol{\theta}}$  is the outwards pointing unit vector normal to the surface. Substituting Eq. (41) we obtain

$$\begin{aligned} \sigma_{-,src}^b = & \frac{E_1 E_2^* \xi}{2\pi^2 n e r_0} \frac{(1 - \epsilon_1)(1 - \epsilon_2^*)}{(1 + \epsilon_1)^2 (1 + \epsilon_2^*)^2} \left[ - (1 - \epsilon_-)(2 + \epsilon_1 + \epsilon_2^*) + (1 - \epsilon_1 \epsilon_2^*) \right. \\ & \left. + \left( \frac{\omega_1 + \omega_2}{\omega_-} \right) (\epsilon_2^* - \epsilon_1) \right] \sin \theta. \end{aligned} \quad (43)$$

We now turn our attention towards the surface of the cylinder and calculate its nonlinear polarization. The expressions for the normal and tangential component of the nonlinear surface DF polarization are given by Eqs. (21) and (26). Both of these expressions were however written down for a semi-infinite surface lying at  $z = 0$  with the  $z$  direction towards the bulk. In order to apply it to the curved cylindrical surface, we assume the thickness of the selvedge to be much smaller than the nominal radius  $r_0$  of the cylinder. This permits us to assume that the surface is locally flat so the results of the dipolium model described in Sec. II A become applicable. We also assume a local Cartesian system on the surface with  $\perp$  denoting the outwards pointing normal direction and  $\parallel$  denoting directions tangential to the surface. The components of the nonlinear surface polarization induced at each point on the surface can then be written as,  $P_{-,i}^s = \chi_{ijk}^s(\omega_1, \bar{\omega}_2) F_{1,j} F_{2,k} + 1 \leftrightarrow 2$ , identical to Eq. (18), where  $\chi_{ijk}^s(\omega_1, \bar{\omega}_2)$  are the components of the local nonlinear surface susceptibility and

$$\mathbf{F}_g(r_s(\theta), \theta) = \mathbf{E}_g(r_s^+(\theta), \theta) = \epsilon_g \mathbf{E}_g^\perp(r_s^-(\theta), \theta) + \mathbf{E}_g^\parallel(r_s^-(\theta), \theta), \quad (44)$$

where  $r_s^\pm = r_s \pm \eta$ ,  $\eta \rightarrow 0^+$  are positions just outside (+) or within (-) the surface. We recall that the fields  $\mathbf{F}_g$  ( $g = 1, 2$ ) are constant across the thin selvedge.

Interpreting Eq. (21) in the locally oriented frame we obtain the normal component of the surface nonlinear polarization

$$\begin{aligned} P_{-, \perp}^s = & \frac{E_1 E_2^*}{32\pi^2 n e} \frac{(1 - \epsilon_1)(1 - \epsilon_2^*)}{(1 + \epsilon_1)(1 + \epsilon_2^*)} \left[ 2a \sin 2\theta + 6\xi a (\sin \theta + \sin 5\theta) \right. \\ & \left. + 8\xi a \sin 3\theta \left\{ \frac{\epsilon_1 - \epsilon_2^*}{(1 + \epsilon_1)(1 + \epsilon_2^*)} \right\} + 8\xi a \sin \theta \left\{ \frac{1 - \epsilon_1 \epsilon_2^*}{(1 + \epsilon_1)(1 + \epsilon_2^*)} \right\} \right], \end{aligned} \quad (45)$$

where the dimensionless parameters  $a$  and  $b$  are given by Eqs. (23) and (29) respectively. Similarly, using Eq. (26) we obtain the tangential component of the surface polarization.

Its spatial variation along the surface yields a *surface originated* nonlinear surface charge  $\sigma_-^s = -\nabla_{\parallel} \cdot \mathbf{P}_{-, \parallel}^s$  given by

$$\begin{aligned} \sigma_-^s = & \frac{E_1 E_2^*}{16\pi^2 n e r_0} b \frac{(1 - \epsilon_1)(1 - \epsilon_2^*)}{(1 + \epsilon_1)(1 + \epsilon_2^*)} \left[ 4 \sin 2\theta - 4\xi \sin \theta + 28\xi \sin 5\theta \right. \\ & \left. + 8\xi \frac{\epsilon_2^* - \epsilon_1}{(1 + \epsilon_1)(1 + \epsilon_2^*)} \left\{ \frac{\omega_1 + \omega_2}{\omega_-} \sin \theta - 3 \sin 3\theta \right\} \right]. \end{aligned} \quad (46)$$

Now that we have calculated its sources, we turn our attention to the calculation of the DF near field. The screened DF scalar potential  $\phi_-$  has  $\rho_{-, \text{src}} = 0$  as an *external bulk* source and the total nonlinear charges induced at the surface  $\sigma_{-, \text{src}}^b$  and  $\sigma_-^s$  as *surface* sources, together with the normal component of the surface polarization  $P_{-, \perp}^s$ , which may be accounted through the boundary conditions. The sources have to be screened by the linear response  $\epsilon_-$  of the particle at the DF frequency. Thus, to obtain the quadratic self-consistent scalar potential we have to solve

$$\nabla^2 \phi_- = \begin{cases} 0, & \text{(outside)} \\ -4\pi \rho_{-, \text{src}} / \epsilon_- = 0, & \text{(inside)} \end{cases} \quad (47)$$

subject to the boundary conditions

$$\phi_-(r_s^+) - \phi_-(r_s^-) = 4\pi P_{-, \perp}^s, \quad (48)$$

and

$$\hat{\mathbf{n}} \cdot \nabla \phi_-(r_s^+) - \epsilon_- \hat{\mathbf{n}} \cdot \nabla \phi_-(r_s^-) = -4\pi(\sigma_{-, \text{src}}^b + \sigma_-^s). \quad (49)$$

Eq. (48) is the discontinuity of the scalar potential due to the presence of the dipole layer  $P_{-, \perp}^s$  across the selvedge. Eq. (49) is the discontinuity of the normal component of the displacement field due to the presence of the nonlinear surface charge. We solve Eq. (47) perturbatively using Eq. (39) (with the subscript  $g = -$ ) to obtain the self-consistent scalar potential at the DF frequency with terms up to linear order in  $\xi$ . The resulting DF self consistent scalar potential  $\phi_-^{\text{out}}$  outside the cylinder is given by

$$\begin{aligned} \frac{\phi_-^{\text{out}}}{E_1 E_2^*} = & \frac{\xi}{\pi n e} \frac{(1 - \epsilon_1)(1 - \epsilon_2^*)}{(1 + \epsilon_1)(1 + \epsilon_2^*)(1 + \epsilon_-)} \left[ \frac{2}{(1 + \epsilon_1)(1 + \epsilon_2^*)} \left\{ -(1 - \epsilon_-)(2 + \epsilon_1 + \epsilon_2^*) \right. \right. \\ & \left. \left. + (1 - \epsilon_1 \epsilon_2^*) + (\epsilon_2^* - \epsilon_1) \left( \frac{\omega_1 + \omega_2}{\omega_-} \right) \right\} - b \frac{1 + 3\epsilon_-}{1 + \epsilon_-} + 2b \frac{\epsilon_2^* - \epsilon_1}{(1 + \epsilon_1)(1 + \epsilon_2^*)} \left( \frac{\omega_1 + \omega_2}{\omega_-} \right) \right. \\ & \left. + \frac{\epsilon_- (3 - \epsilon_-) a}{4} \frac{1}{1 + \epsilon_-} + \frac{\epsilon_-}{4} \left\{ 3a + \frac{4a(1 - \epsilon_1 \epsilon_2^*)}{(1 + \epsilon_1)(1 + \epsilon_2^*)} \right\} \right] \frac{r_0}{r} \sin \theta \\ & + \frac{1}{4\pi n e} \frac{(1 - \epsilon_1)(1 - \epsilon_2^*)}{(1 + \epsilon_1)(1 + \epsilon_2^*)(1 + \epsilon_-)} [\epsilon_- a + 2b] \frac{r_0^2}{r^2} \sin 2\theta + \dots \end{aligned} \quad (50)$$

We must remark that terms corresponding to higher order multipoles are present in this second order potential; however, they are of linear order in deformation and smaller than the dipole by at least  $r_0/\lambda$ . Comparing Eq. (50) with the general expression of the 2D scalar potential

$$\phi_-^{\text{out}} = 2p_{-,y} \frac{\sin \theta}{r} + Q_{-,xy} \frac{\sin 2\theta}{r^2} + \dots \quad (51)$$

we identify the DF 2D dipolar and quadrupolar moments per unit length  $p_{-,i}$  and  $Q_{-,ij}$ . The quadratic dipole contributes only for a non-zero deformation  $\xi$  while the quadrupolar response  $Q_{xy}$  is independent of  $\xi$  and would exist even for a non-deformed circular cylinder. We define dipolar and quadrupolar hyperpolarizability tensors through  $p_{-,i} = \gamma_{ijk}^d(\omega_1, \bar{\omega}_2) E_{1,j}^{\text{ex}} (E_{2,k}^{\text{ex}})^* + 1 \leftrightarrow 2$  and  $Q_{-,ij} = \gamma_{ijkl}^Q(\omega_1, \bar{\omega}_2) E_{1,k}^{\text{ex}} (E_{2,l}^{\text{ex}})^* + 1 \leftrightarrow 2$ . Together with Eq. (51), they allow us to write the DF moments as

$$p_{-,y} = [\gamma_{yxy}^d(\omega_1, \bar{\omega}_2) + \gamma_{yyx}^d(\bar{\omega}_2, \omega_1)] E_{1,x} E_{2,y}^* = \gamma^d(\omega_1, \bar{\omega}_2) E_{1,x} E_{2,y}^*, \quad (52)$$

$$Q_{-,xy} = [\gamma_{xyxy}^Q(\omega_1, \bar{\omega}_2) + \gamma_{xyyx}^Q(\bar{\omega}_2, \omega_1)] E_{1,x} E_{2,y}^* = \gamma^Q(\omega_1, \bar{\omega}_2) E_{1,x} E_{2,y}^*, \quad (53)$$

where we define

$$\gamma^d(\omega_1, \bar{\omega}_2) = \gamma_{yxy}^d(\omega_1, \bar{\omega}_2) + \gamma_{yyx}^d(\bar{\omega}_2, \omega_1) = 2\gamma_{yxy}^d(\omega_1, \bar{\omega}_2) = 2\gamma_{yyx}^d(\bar{\omega}_2, \omega_1) \quad (54)$$

and

$$\gamma^Q(\omega_1, \bar{\omega}_2) = \gamma_{xyxy}^Q(\omega_1, \bar{\omega}_2) + \gamma_{xyyx}^Q(\bar{\omega}_2, \omega_1) = 2\gamma_{xyxy}^Q(\omega_1, \bar{\omega}_2) = 2\gamma_{xyyx}^Q(\bar{\omega}_2, \omega_1) \quad (55)$$

using the intrinsic permutation symmetry  $\gamma_{yxy}^d(\omega_1, \bar{\omega}_2) = \gamma_{yyx}^d(\bar{\omega}_2, \omega_1)$  and  $\gamma_{xyxy}^Q(\omega_1, \bar{\omega}_2) = \gamma_{xyyx}^Q(\bar{\omega}_2, \omega_1)$ . Comparing Eqs. (52) and (53) with Eqs. (50) and (51), we identify the DF hyperpolarizabilities

$$\begin{aligned} \gamma^d(\omega_1, \bar{\omega}_2) &= \frac{\xi r_0}{2\pi n e} \frac{(1 - \epsilon_1)(1 - \epsilon_2^*)}{(1 + \epsilon_1)(1 + \epsilon_2^*)(1 + \epsilon_-)} \left[ \frac{2}{(1 + \epsilon_1)(1 + \epsilon_2^*)} \left\{ - (1 - \epsilon_-)(2 + \epsilon_1 + \epsilon_2^*) \right. \right. \\ &\quad \left. \left. + (1 - \epsilon_1 \epsilon_2^*) + (\epsilon_2^* - \epsilon_1) \left( \frac{\omega_1 + \omega_2}{\omega_-} \right) \right\} - b \frac{1 + 3\epsilon_-}{1 + \epsilon_-} + 2b \frac{(\epsilon_2^* - \epsilon_1)}{(1 + \epsilon_1)(1 + \epsilon_2^*)} \left( \frac{\omega_1 + \omega_2}{\omega_-} \right) \right. \\ &\quad \left. + \frac{\epsilon_- (3 - \epsilon_-) a}{4} \frac{1 + \epsilon_-}{1 + \epsilon_-} + \frac{\epsilon_-}{4} \left\{ 3a + \frac{4a(1 - \epsilon_1 \epsilon_2^*)}{(1 + \epsilon_1)(1 + \epsilon_2^*)} \right\} \right], \quad (56) \end{aligned}$$

$$\gamma^Q(\omega_1, \bar{\omega}_2) = \frac{r_0^2}{4\pi n e} \frac{(1 - \epsilon_1)(1 - \epsilon_2^*)}{(1 + \epsilon_1)(1 + \epsilon_2^*)(1 + \epsilon_-)} (a\epsilon_- + 2b). \quad (57)$$

We now turn our attention towards the calculation of the nonlinear magnetic dipole moment induced in the nanocylinder, the density of which is given by Eq. (13). The total



magnetic moment per unit length induced within the nanocylinder can be obtained by integrating Eq. (13) across the cross-section,

$$\mathbf{m}_-^{(2)} = \int_0^{2\pi} \int_0^{r_s(\theta)} \boldsymbol{\mu}_-^{(2)} r dr d\theta. \quad (58)$$

Substituting the linear fields obtained from Eq. (40) in Eq. (13), we obtain

$$\mathbf{m}_-^{(2)} = -\frac{i}{ce} \frac{E_1 E_2^* r_0^2}{8\pi n^2} (\omega_1 + \omega_2) \frac{(1 - \epsilon_1)(1 - \epsilon_2^*)}{(1 + \epsilon_1)(1 + \epsilon_2^*)} \hat{\mathbf{z}}. \quad (59)$$

Defining  $m_{-,z} = \gamma_{zxy}^m(\omega_1, \bar{\omega}_2) E_{1,x} E_{2,y}^* + 1 \leftrightarrow 2$ , and following a procedure similar to Eq. (52), we identify the quadratic magnetic dipolar hyperpolarizability  $\gamma^m(\omega_1, \bar{\omega}_2)$ . We obtain

$$\gamma^m(\omega_1, \bar{\omega}_2) = 2\gamma_{zxy}^m(\omega_1, \bar{\omega}_2) = -\frac{i}{ce} \frac{r_0^2}{8\pi n^2} (\omega_1 + \omega_2) \frac{(1 - \epsilon_1)(1 - \epsilon_2^*)}{(1 + \epsilon_1)(1 + \epsilon_2^*)}. \quad (60)$$

The limit  $\omega_2 \rightarrow \omega_1$ ,  $\omega_- \rightarrow 0$  of Eqs. (56), (57) and (60) yields the OR hyperpolarizabilities, i.e. the second order response of the nanocylinder for the nonlinear rectification process. The SF hyperpolarizabilities, corresponding to the frequency  $\omega_+ = \omega_1 + \omega_2$ , can be easily read from Eqs. (56), (57) and (60) after substituting  $\bar{\omega}_2$  by  $\omega_2$ ,  $\epsilon_-$  by  $\epsilon_+$ , and taking the complex conjugate of the permittivity, i.e. changing  $\epsilon_2^*$  to  $\epsilon_2$ , yielding

$$\begin{aligned} \gamma^d(\omega_1, \omega_2) = & \frac{\xi r_0}{2\pi n e} \frac{(1 - \epsilon_1)(1 - \epsilon_2)}{(1 + \epsilon_1)(1 + \epsilon_2)(1 + \epsilon_+)} \left[ \frac{2}{(1 + \epsilon_1)(1 + \epsilon_2)} \left\{ - (1 - \epsilon_+)(2 + \epsilon_1 + \epsilon_2) \right. \right. \\ & \left. \left. + (1 - \epsilon_1 \epsilon_2) + (\epsilon_2 - \epsilon_1) \left( \frac{\omega_1 - \omega_2}{\omega_+} \right) \right\} - b \frac{1 + 3\epsilon_+}{1 + \epsilon_+} + 2b \frac{\epsilon_2 - \epsilon_1}{(1 + \epsilon_1)(1 + \epsilon_2)} \left( \frac{\omega_1 - \omega_2}{\omega_+} \right) \right. \\ & \left. + \frac{\epsilon_+ (3 - \epsilon_+) a}{4} + \frac{\epsilon_+}{4} \left\{ 3a + \frac{4a(1 - \epsilon_1 \epsilon_2)}{(1 + \epsilon_1)(1 + \epsilon_2)} \right\} \right], \quad (61) \end{aligned}$$

$$\gamma^Q(\omega_1, \omega_2) = \frac{r_0^2}{4\pi n e} \frac{(1 - \epsilon_1)(1 - \epsilon_2)}{(1 + \epsilon_1)(1 + \epsilon_2)(1 + \epsilon_+)} [\epsilon_+ a + 2b], \quad (62)$$

and

$$\gamma^m(\omega_1, \omega_2) = -\frac{i}{ce} \frac{r_0^2}{8\pi n^2} (\omega_1 - \omega_2) \frac{(1 - \epsilon_1)(1 - \epsilon_2)}{(1 + \epsilon_1)(1 + \epsilon_2)}. \quad (63)$$

The degenerate SH case can be obtained from Eqs. (61) and (62) when the input frequencies are equal, i.e.  $\omega_2 = \omega_1$ . Note, that the magnetic hyperpolarizability given by Eq. (63) would be zero for the SH case.

In order to calculate the other non-zero components of the hyperpolarizabilities, we repeat the calculations above but with different polarization of the incident fields to find all the

non-zero components of the hyperpolarizabilities,

$$\begin{aligned}\gamma_{bab}^d(\omega_c, \omega_d) &= \gamma_{bba}^d(\omega_c, \omega_d) = -\gamma_{aaa}^d(\omega_c, \omega_d) = \gamma_{abb}^d(\omega_c, \omega_d) \\ &= \gamma^d(\omega_c, \omega_d)/2 = \gamma^d(\omega_d, \omega_c)/2,\end{aligned}\tag{64}$$

$$\begin{aligned}\gamma_{abab}^Q(\omega_c, \omega_d) &= \gamma_{abba}^Q(\omega_c, \omega_d) = -\gamma_{aabb}^Q(\omega_c, \omega_d) = \gamma_{aaaa}^Q(\omega_c, \omega_d) \\ &= \gamma^Q(\omega_c, \omega_d)/2 = \gamma^Q(\omega_d, \omega_c)/2,\end{aligned}\tag{65}$$

$$\gamma_{zab}^m(\omega_c, \omega_d) = \gamma_{zba}^m(\omega_d, \omega_c) = \gamma^m(\omega_c, \omega_d)/2 = -\gamma^m(\omega_d, \omega_c)/2\tag{66}$$

where the pair of indices  $(a, b)$  can take the values  $(x, y)$  or  $(y, x)$ , and the pair of frequencies  $(\omega_c, \omega_d)$  can take independently the values  $(\omega_1, \omega_2)$  or  $(\omega_2, \omega_1)$ . All other components are zero for our system.

### C. SF/DF efficiency

We now focus on the calculation of the electromagnetic fields in the radiation zone and the efficiency of DFG/SFG from the nanocylinder. Following a procedure similar to the 3D case, one can write down the expressions for the radiated electromagnetic fields in 2D due to a localized distribution of charges and currents [14]. The magnetic and electric far fields radiated at the SF/DF frequency are

$$\mathbf{B}_\pm = (1 + i)k_\pm^{3/2} \left( (\hat{\mathbf{r}} \times \mathbf{p}_\pm) - \hat{\mathbf{r}} \times (\hat{\mathbf{r}} \times \mathbf{m}_\pm) - \frac{i}{4}k_\pm(\hat{\mathbf{r}} \times (\mathbf{Q}_\pm \cdot \hat{\mathbf{r}})) \right) e^{ik_\pm r} \sqrt{\frac{\pi}{r}},\tag{67}$$

$$\mathbf{E}_\pm = \mathbf{B}_\pm \times \hat{\mathbf{r}},\tag{68}$$

considering the dominant electric-dipolar, magnetic-dipolar, and electric-quadrupolar contributions, where  $k_\pm$  is the free wavenumber corresponding to the frequency  $\omega_\pm$ ,  $\hat{\mathbf{r}}$  is the outward pointing unit vector in the direction of observation, and  $\mathbf{p}_\pm$ ,  $\mathbf{Q}_\pm$  and  $\mathbf{m}_\pm$  are given by Eqs. (52), (53) and (59) respectively. In the appendix of Ref. [14] the electric dipolar and quadrupolar contributions to the radiated fields were presented; the magnetic dipolar contribution is discussed in our Appendix. The time averaged power radiated per unit angle in the direction  $\theta$  is

$$\frac{dP_\pm}{d\theta} = \frac{rc}{2\pi} \text{Re}[\mathbf{E}_\pm \times \mathbf{B}_\pm^*] \cdot \hat{\mathbf{r}},\tag{69}$$

which after substituting Eqs. (67) and (68) becomes

$$\begin{aligned} \frac{d\mathcal{P}_\pm}{d\theta} = ck_\pm^3 |E_1 E_2|^2 [ & |\gamma_\pm^d|^2 \cos^2 \theta + |\gamma_\pm^m|^2 + \frac{k_\pm^2}{16} |\gamma_\pm^Q|^2 \cos^2 2\theta + 2 \operatorname{Re}(\gamma_\pm^d \gamma_\pm^{m*}) \cos \theta \\ & - \frac{k_\pm}{2} \operatorname{Im}(\gamma_\pm^m \gamma_\pm^{Q*}) \cos 2\theta - \frac{k_\pm}{2} \operatorname{Im}(\gamma_\pm^d \gamma_\pm^{Q*}) \cos \theta \cos 2\theta]. \end{aligned} \quad (70)$$

Here, we introduce the compact notation  $\gamma_+^\alpha \equiv \gamma^\alpha(\omega_1, \omega_2)$  and  $\gamma_-^\alpha \equiv \gamma^\alpha(\omega_1, \bar{\omega}_2)$  with  $\alpha = d, m, Q$ . Integrating we obtain the total SF/DF power radiated per unit length,

$$\mathcal{P}_\pm = \pi ck_\pm^3 |E_1 E_2|^2 \left[ |\gamma_\pm^d|^2 + 2|\gamma_\pm^m|^2 + \frac{k_\pm^2}{16} |\gamma_\pm^Q|^2 \right]. \quad (71)$$

The efficiency of the SFG/DFG process, defined as

$$\mathcal{R}_\pm = \frac{\mathcal{P}_\pm}{I_1 I_2}, \quad (72)$$

where  $I_g = (c/2\pi)|E_g|^2$  ( $g = 1, 2$ ) are the intensities of the incident waves, is

$$\mathcal{R}_\pm = \frac{\pi^3}{1024} \frac{k_\pm^3}{c} \left[ |\gamma_\pm^d|^2 + 2|\gamma_\pm^m|^2 + \frac{k_\pm^2}{16} |\gamma_\pm^Q|^2 \right], \quad (73)$$

### III. RESULTS AND DISCUSSIONS

Fig. 2 illustrates the absolute value of the electric-dipolar, electric-quadrupolar, and the magnetic-dipolar hyperpolarizabilities  $\gamma^\alpha$ ,  $\alpha = d, Q, m$  given by Eqs. (56), (57) and (60) to (63) respectively, for a deformed cylinder made up of an insulator with dielectric permittivity given by Eq. (24) with  $\omega_L = \sqrt{2}\omega_T$  and  $\tau = 20/\omega_T$ , as used in Fig. 1. We allow both the input frequencies to take negative and positive values to cover all three-wave mixing processes, namely, SFG, DFG, SHG, and OR, by identifying  $\gamma^\alpha(\omega_1, \omega_2) = \gamma_+^\alpha$  when both frequencies are positive,  $\gamma^\alpha(\omega_1, \omega_2) = \gamma_-^\alpha$  when  $\omega_1 > 0$  and  $\omega_2 < 0$ , and  $\gamma^\alpha(\omega_1, \omega_2) = (\gamma^\alpha(-\omega_1, -\omega_2))^*$  when  $\omega_1 < 0$ . We show both 3D surface plots and 2D color maps to better convey the qualitative and quantitative nature of the results. All three hyperpolarizabilities show strong resonant ridges when either input frequency is equal to the surface plasmon polariton (SPP) frequency or its additive inverse,  $\omega_g = \pm\omega_{\text{spp}} = \pm\sqrt{3/2}\omega_T$ . Intense diagonal ridges occur for  $\gamma^d$  and  $\gamma^Q$ , but not in  $\gamma^m$ , when the sum of the two incident frequencies resonates with the SPP. There are further peaks when any of the two ridges meet, for which two of the resonant conditions are fulfilled jointly. The first quadrant corresponds to SFG, the fourth with DFG, and the third and second replicate these processes inverting the signs of all participating

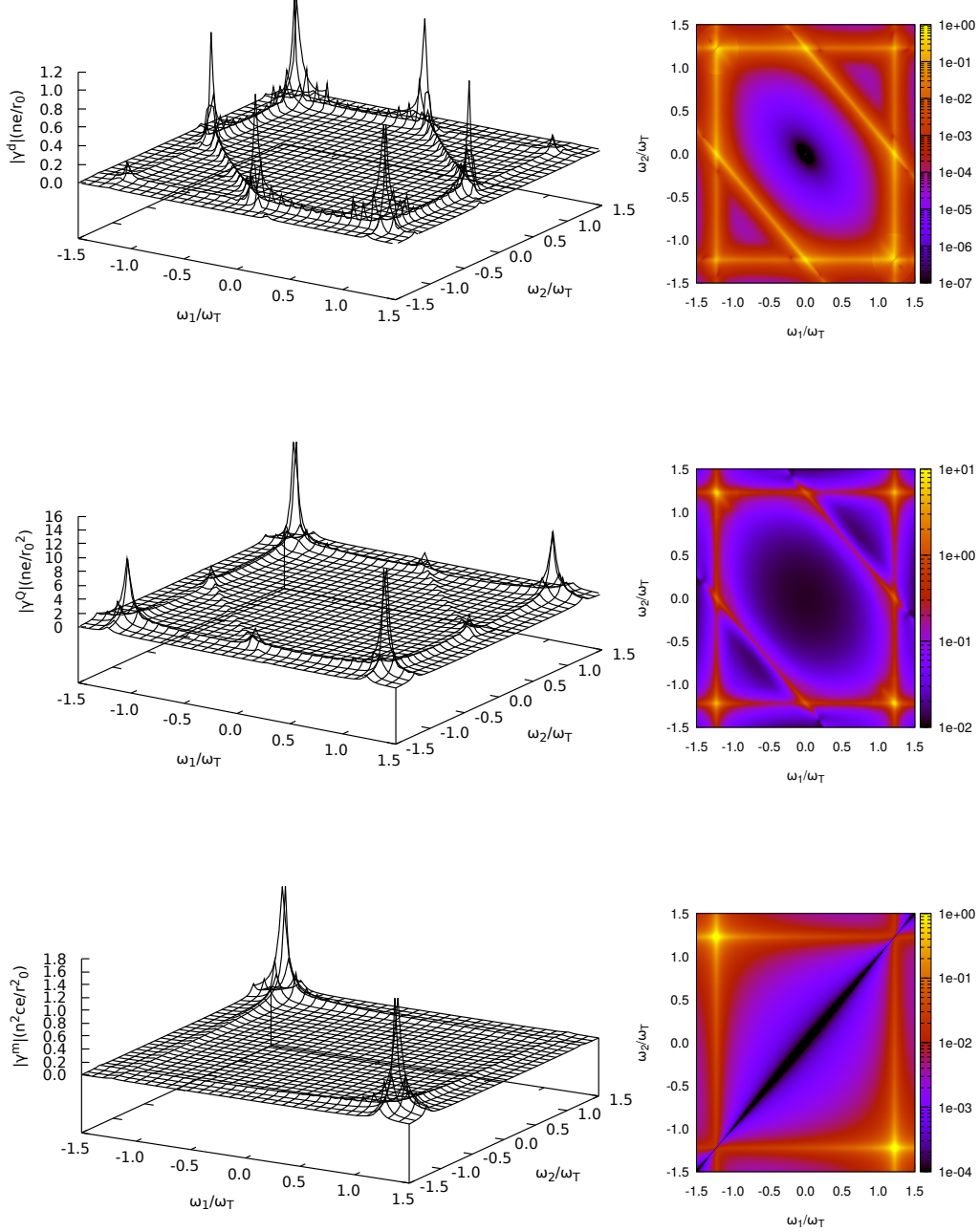


FIG. 2. Normalized absolute value of the electric dipolar  $\gamma^d$  (top panels), the electric quadrupolar (middle panels)  $\gamma^Q$  and the magnetic dipolar (bottom panels)  $\gamma^m$  hyperpolarizabilities for an infinitely long and thin deformed dielectric cylinder as a function of the fundamental frequencies  $\omega_1$  and  $\omega_2$ . The permittivity is given by Eq. (24) with  $\omega_L = \sqrt{2}\omega_T$  and  $\tau = 20/\omega_T$ . The deformation is  $\xi = 0.03$ . 3D surface plots are displayed in the left panels and the respective 2D color maps in the right panels. The regions where both frequencies have the same signs correspond to SFG and those with opposite signs to DFG.

frequencies. The large peak observed in the fourth quadrant corresponds to DFG close to OR, where both the incident frequencies are simultaneously SPP resonant. The response along the diagonal  $\omega_1 = \omega_2$  corresponds to SHG. Notice that in this case we cross a diagonal ridge when the fundamental frequency is the subharmonic of the SPP resonance and meet a peak when the fundamental reaches the resonance condition. The quadratic magnetic dipole is absent along the SH line. The horizontal, vertical, and diagonal ridges are much weaker than the doubly resonant peaks for both the quadrupolar and the dipolar response. We also explored the absolute values of  $\gamma^d$ ,  $\gamma^Q$  and  $\gamma^m$  for larger lifetimes (not shown). As expected, we obtained a similar structure with much narrower and sharper peaks and ridges. In Fig. 3, we show a closeup of  $\gamma^d$  around  $\omega_1 = -\omega_2 = \omega_{\text{spp}}$ , corresponding to DFG process with a small difference in frequency. Notice that when the two input frequencies are exactly equal and opposite,  $\omega_- = 0$ , the second order response is about an order of magnitude lower than for neighboring points, for which  $\omega_-$  is small but finite. Thus, the electric-dipolar response of the system for OR is smaller than its DF response. No such behavior is observed for the quadrupolar nor the magnetic dipolar hyperpolarizability.

In Fig. 4 we present the SFG/DFG dimensionless efficiencies

$$\mathcal{R}'_{\pm} = cr_0(ne)^2\mathcal{R}_{\pm} \quad (74)$$

corresponding to the same cylinder as in Fig. 2. We obtain a structure similar to that for the hyperpolarizabilities, with vertical, horizontal and diagonal ridges and peaks where two ridges meet. Note that the main peak correspond to a SHG process where both input frequencies are resonant with the SPP of the cylinder, followed in intensity by SFG/DFG peaks where one input frequency is close to zero. The SHG at the SPP subharmonic is relatively small and there is no peak corresponding to OR where both frequencies are SPP resonant. Nevertheless, there is a substantial DFG radiation when one frequency is SPP resonant and the other is close to the resonance, indicating a possible application towards the generation of THz radiation.

In Fig. 5 we show the regions of frequency  $(\omega_1, \omega_2)$  space where the largest contribution to the nonlinear efficiency is electric-dipolar, magnetic-dipole or electric quadrupolar. Notice that the electric dipole is dominant when  $\omega_+$  resonates with the SPP, and that the electric quadrupole dominates along the SHG line, except at the subharmonic of the SPP. The rest of the frequency space is dominated by the magnetic dipole.

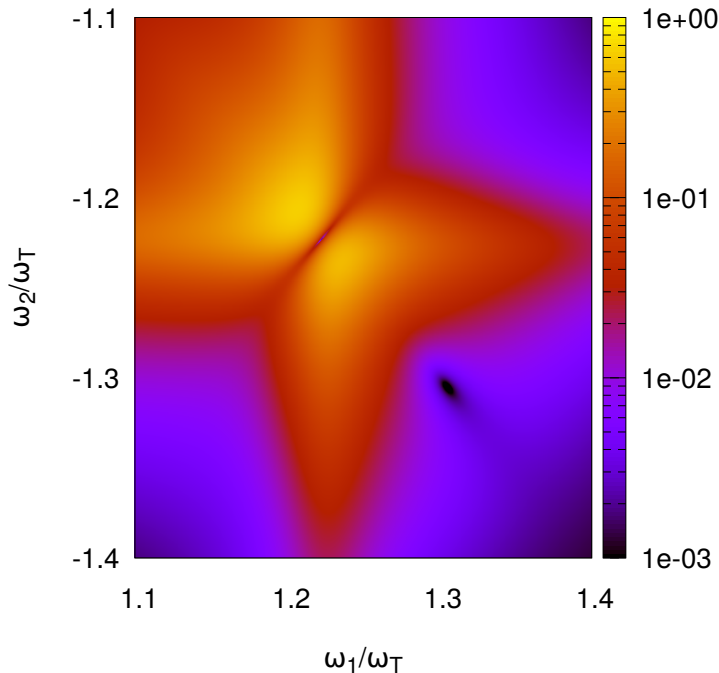


FIG. 3. High resolution 2D color map of the normalized dipolar hyperpolarizability  $|\gamma^d|$ , shown in Fig. 2, close to the resonance around the region  $\omega_1 \approx \omega_2 \approx \omega_{\text{spp}}$ , with  $\omega_2$  negative.

In Fig. 6, we plot the normalized 2D angular radiation pattern of the same cylinder as in Fig. 2 and Fig. 4 in the vicinity of resonances corresponding to the regions marked in Fig. 4. Even though the calculation corresponds to a small deformation,  $\xi = 0.03$ , we observe a strong competition between the electric-dipolar, magnetic-dipolar, and quadrupolar contributions. Thus, around the region *a* of Fig. 4, in Fig. 6 we obtain an almost isotropic radiation pattern along the  $x - y$  plane, corresponding to the radiation of a magnetic dipole oriented along  $z$ . As we move vertically towards point *b* there is a competition between electric and magnetic dipolar radiation, which yields a partially directional radiation and as we approach *c* the radiation has mostly the two lobed electric-dipolar form. As we proceed to *d* the radiation becomes a mixture of magnetic-dipolar and electric-quadrupolar and the latter dominates close to *e*. Moving towards *f* and *g* the pattern becomes again electric-dipolar and finally, close to *h* it becomes a mixture of electric dipolar and quadrupolar contributions. We must remark here that though Fig. 4 is symmetric under the interchange  $\omega_1 \leftrightarrow \omega_2$ , we purposely chose points *c* and *g* that are not equivalent, in order to show the richness of the radiation patterns. Similarly, we chose *d* nonequivalent to *f*. An animation illustrating the

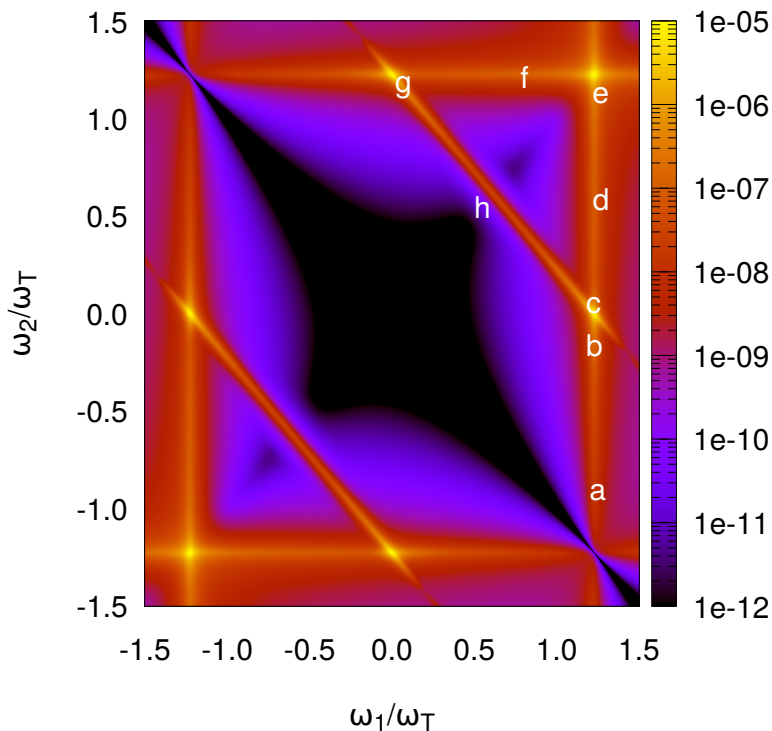


FIG. 4. Dimensionless efficiency for three-wave mixing processes for the same dielectric cylinder as in Fig. 2 as function of normalized input frequencies  $\omega_g/\omega_T$  for  $g = 1, 2$  for deformation  $\xi = 0.03$  and  $r_0/\lambda_T = 0.01$ .

evolution of the generated radiation pattern as we vary continuously the input frequencies is available in the supplementary video file[42].

#### IV. CONCLUSIONS

We developed a formalism to calculate *analytically* all three-wave mixing processes, sum and difference frequency generation, second harmonic generation [14] and optical rectification, for slightly deformed thin cylinders with a simple noncentrosymmetric cross-section. Our theory was developed in  $2D$  within the long-wavelength approximation, assuming translational symmetry along the axis of the cylinder, and is of a perturbative nature, assuming the geometry is controlled by a small deformation parameter. We first generalized the *dipolium* model to calculate the DF response of a semi-infinite homogeneous media, and used the results to compute the bulk and surface contributions to the DF polarization of the

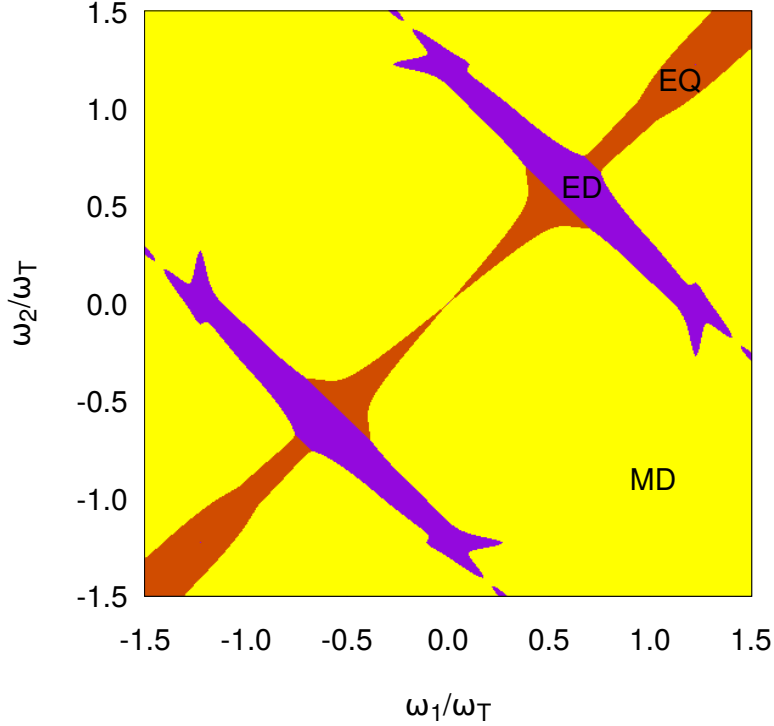


FIG. 5. Different regions of frequency space colored according to the nature of the largest contribution to the non-linear efficiency shown in Fig. 4, electric-dipolar (ED), magnetic-dipolar (MD), and electric-quadrupolar (EQ).

cylinder, assuming its surface is smooth and thus locally flat. This polarization is a source for the near DF fields from which we identified the total DF electric dipole  $\mathbf{p}_-$  and quadrupole  $\mathbf{Q}_-$ , and we also obtained the nonlinear magnetic dipole  $\mathbf{m}_-$ . We thus obtained all the finite components of the corresponding hyperpolarizability tensors which were of order one in the deformation parameter for the electric dipolar case and of order zero in the other cases. We also calculated the radiation fields, radiation patterns and conversion efficiency. A simple extension allowed us to also obtain the induced moments, hyperpolarizabilities and the radiation corresponding to SF, SH and OR.

Our results are written in terms of the linear dielectric response of the system evaluated at the relevant frequencies. We illustrated them by calculating and analyzing the SF/DF hyperpolarizabilities, radiation patterns and efficiencies for a model harmonic dielectric, and we interpreted their resonant structure, related to the excitation of surface plasmon



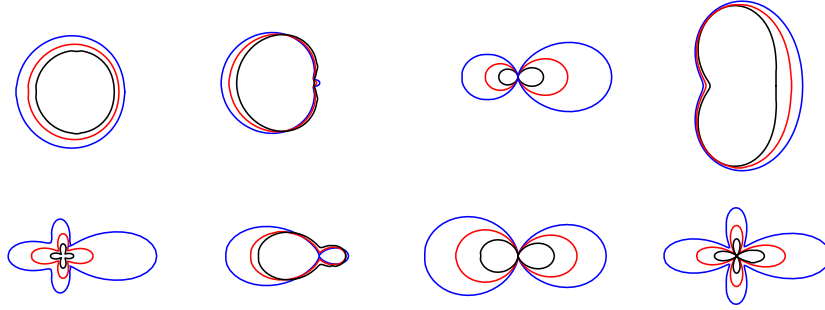


FIG. 6.  $2D$  angular radiation patterns for the same dielectric cylinder as in Fig. 4 for different input frequencies  $\omega_1$  and  $\omega_2$ . Each set of patterns corresponds to the region around the points marked in Fig. 4: from left to right a-d (top row), and e-h (bottom row). For the patterns a-e we set  $\omega_1 = \omega_{\text{spp}}$  while varying  $\omega_2$ , i.e. we traverse along the vertical line at resonance, f lies on the horizontal line where  $\omega_2 = \omega_{\text{spp}}$ . We choose both the input frequencies to vary along the diagonal resonance for regions g and h.

polaritons at the input and/or output frequencies. We found a strong DFG when  $\omega_1 \approx \omega_{\text{spp}} \approx \omega_2$ , corresponding to a small but finite  $\omega_-$ , suggesting that our system might yield an efficient generation of radiation in the THz regime. We further identified the regions in the frequency space where different multipolar contributions became dominant and we illustrated them through calculations of the corresponding radiation patterns. The nonlinear magnetic dipole moment was found to dominate for most frequency combinations, but it is zero for the SH case. Our results show that for some  $\omega_1, \omega_2$  frequency combinations, the electric-dipolar contribution may become comparable to the electric-quadrupolar or the magnetic-dipolar contributions even for very slightly deformed cylinders.

In summary, we developed an analytical formalism that allowed us to explore all three-wave mixing processes at  $2D$  nanocylinders made up of centrosymmetric materials but with a noncentrosymmetric geometry. Although we developed the model for an harmonic *dipolium* model, the results are written in terms of the dielectric function of the material evaluated at the relevant input and output frequencies. Thus, by substituting the appropriate response functions, our results may be applied to arbitrary dielectrics. Furthermore, it may be shown that the results agree with those of a local *jellium* model, so they may also be applied to met-

als [35]. Our theory does not take into account effects related to crystal structure, the presence of surface states, and surface reconstructions and relaxation. Nevertheless, our results allow a quantification of the expected efficiency of the different processes, and, in particular, they show that electric electric dipolar contributions may dominate the quadrupolar and magnetic dipolar ones at certain frequency combinations even for very small deformations. Thus, ordinary centrosymmetric materials textured with noncentrosymmetric patterns may provide competitive sources of optical sum and difference frequency generation for processes such as conversion of light into the THz regime. Furthermore, our model provides analytical expressions against which numerical computational schemes may be tested.

## ACKNOWLEDGMENTS

This work was supported by DGAPA-UNAM under grant IN111119 (WLM) and by CONACyT (RS). We acknowledge useful discussions with B. S. Mendoza.

## APPENDIX

In this Appendix, we calculate the electromagnetic fields radiated in  $2D$  by a magnetic dipole. A detailed description of the derivation is not presented here as a similar calculation was discussed in the Appendix of Ref. [14], where radiation from an electric dipole and a quadrupole were considered. Eq. (A6) of Ref. [14] is an expression for the vector potential in  $2D$  radiated by a harmonically varying monochromatic current distribution  $\mathbf{J}(\mathbf{r}, t)$ , expressed as a power series in the diameter of the system. The second term of this series is

$$\mathbf{A}^{(1)}(\mathbf{r}) = \frac{1}{c} \sqrt{\frac{2\pi}{kr}} e^{i\pi/4} e^{ikr} (-ik) \int d^2r' \mathbf{J}(\mathbf{r}') (\hat{\mathbf{r}} \cdot \mathbf{r}'), \quad (\text{A.75})$$

Its integrand can be written as the sum of a symmetric and an antisymmetric part,  $\mathbf{J}(\mathbf{r}')(\hat{\mathbf{r}} \cdot \mathbf{r}') = (1/2)[\mathbf{J}(\mathbf{r}')(\hat{\mathbf{r}} \cdot \mathbf{r}') + \mathbf{r}'(\hat{\mathbf{r}} \cdot \mathbf{J}(\mathbf{r}'))] + (1/2)[\mathbf{J}(\mathbf{r}')(\hat{\mathbf{r}} \cdot \mathbf{r}') - \mathbf{r}'(\hat{\mathbf{r}} \cdot \mathbf{J}(\mathbf{r}'))]$ . The former yields the electric quadrupolar radiation while latter corresponds to the contribution of the magnetic dipole, which can be written as

$$\mathbf{A}^m(\mathbf{r}) = \sqrt{\frac{2\pi}{kr}} e^{i\pi/4} e^{ikr} (ik) \hat{\mathbf{r}} \times \mathbf{m}, \quad (\text{A.76})$$

where  $\mathbf{m}$  is the magnetic dipole moment per unit length,

$$\mathbf{m} = \frac{1}{2c} \int d^2r' \mathbf{r}' \times \mathbf{J}(\mathbf{r}'). \quad (\text{A.77})$$

As mentioned in Ref. [14], we may obtain the corresponding electromagnetic radiation field as  $\mathbf{B}^m = ik\hat{\mathbf{r}} \times \mathbf{A}^m$  and  $\mathbf{E}^m = \mathbf{B}^m \times \hat{\mathbf{r}}$ .

- 
- [1] J. M. Dudley, G. Genty, and S. Coen, Supercontinuum generation in photonic crystal fiber, *Rev. Mod. Phys.* **78**, 1135 (2006).
  - [2] A. Yariv, Four wave nonlinear optical mixing as real time holography, *Optics Communications* **25**, 23 (1978).
  - [3] N. M. Kroll, Parametric amplification in spatially extended media and application to the design of tuneable oscillators at optical frequencies, *Phys. Rev.* **127**, 1207 (1962).
  - [4] W. Kaiser, *Ultrashort Laser Pulses*.
  - [5] I.-Y. Park, S. Kim, J. Choi, D.-H. Lee, Y.-J. Kim, M. F. Kling, M. I. Stockman, and S.-W. Kim, Plasmonic generation of ultrashort extreme-ultraviolet light pulses, *Nature Photonics* **5**, 677 (2011).
  - [6] F. Monticone and A. Alù, Metamaterial, plasmonic and nanophotonic devices, *Reports on Progress in Physics* **80**, 036401 (2017).
  - [7] D. Smirnova and Y. S. Kivshar, Multipolar nonlinear nanophotonics, *Optica* **3**, 1241 (2016).
  - [8] M. Kauranen and A. V. Zayats, Nonlinear plasmonics, *Nature Photonics* **6**, 737 (2012).
  - [9] R. Czaplicki, J. Mäkitalo, R. Siikanen, H. Husu, J. Lehtolahti, M. Kuittinen, and M. Kauranen, Second-harmonic generation from metal nanoparticles: Resonance enhancement versus particle geometry, *Nano Letters* **15**, 530 (2015), pMID: 25521745, <https://doi.org/10.1021/nl503901e>.
  - [10] S. Liu, M. B. Sinclair, S. Saravi, G. A. Keeler, Y. Yang, J. Reno, G. M. Peake, F. Setzpfandt, I. Staude, T. Pertsch, and I. Brener, Resonantly enhanced second-harmonic generation using iii-v semiconductor all-dielectric metasurfaces, *Nano Letters* **16**, 5426 (2016), pMID: 27501472, <https://doi.org/10.1021/acs.nanolett.6b01816>.
  - [11] B. Metzger, M. Hentschel, T. Schumacher, M. Lippitz, X. Ye, C. B. Murray, B. Knabe, K. Buse, and H. Giessen, Doubling the efficiency of third harmonic generation by positioning ito nanocrystals into the hot-spot of plasmonic gap-antennas, *Nano Letters* **14**, 2867 (2014), pMID: 24730433, <https://doi.org/10.1021/nl500913t>.
  - [12] V. F. Gili, L. Carletti, A. Locatelli, D. Rocco, M. Finazzi, L. Ghirardini, I. Favero, C. Gomez,

- A. Lemaître, M. Celebrano, C. D. Angelis, and G. Leo, Monolithic algaas second-harmonic nanoantennas, *Opt. Express* **24**, 15965 (2016).
- [13] U. R. Meza, B. S. Mendoza, and W. L. Mochán, Second-harmonic generation in nanostructured metamaterials, *Phys. Rev. B* **99**, 125408 (2019).
- [14] R. Singla and W. L. Mochán, Analytical theory of second harmonic generation from a nanowire with noncentrosymmetric geometry, *Phys. Rev. B* **99**, 125418 (2019).
- [15] W. Wenseleers, F. Stellacci, T. Meyer-Friedrichsen, T. Mangel, C. A. Bauer, S. J. K. Pond, S. R. Marder, and J. W. Perry, Five orders-of-magnitude enhancement of two-photon absorption for dyes on silver nanoparticle fractal clusters, *The Journal of Physical Chemistry B* **106**, 6853 (2002), <https://doi.org/10.1021/jp014675f>.
- [16] M. Lippitz, M. A. van Dijk, and M. Orrit, Third-harmonic generation from single gold nanoparticles, *Nano Letters* **5**, 799 (2005), pMID: 15826131, <https://doi.org/10.1021/nl0502571>.
- [17] A. Yariv and D. M. Pepper, Amplified reflection, phase conjugation, and oscillation in degenerate four-wave mixing, *Opt. Lett.* **1**, 16 (1977).
- [18] V. Boyer, A. M. Marino, R. C. Pooser, and P. D. Lett, Entangled images from four-wave mixing, *Science* **321**, 544 (2008), <https://science.sciencemag.org/content/321/5888/544.full.pdf>.
- [19] N. Ji, K. Zhang, H. Yang, and Y.-R. Shen, Three-dimensional chiral imaging by sum-frequency generation, *Journal of the American Chemical Society* **128**, 3482 (2006), pMID: 16536497, <https://doi.org/10.1021/ja057775y>.
- [20] A. A. Pikalov, D. Ngo, H. J. Lee, T. R. Lee, and S. Baldelli, Sum frequency generation imaging microscopy of self-assembled monolayers on metal surfaces: Factor analysis of mixed monolayers, *Analytical Chemistry* **91**, 1269 (2019), <https://doi.org/10.1021/acs.analchem.8b01840>.
- [21] L. Moreaux, O. Sandre, and J. Mertz, Membrane imaging by second-harmonic generation microscopy, *J. Opt. Soc. Am. B* **17**, 1685 (2000).
- [22] W. P. Dempsey, S. E. Fraser, and P. Pantazis, Shg nanoprobe: Advancing harmonic imaging in biology, *BioEssays* **34**, 351 (2012), <https://onlinelibrary.wiley.com/doi/pdf/10.1002/bies.201100106>.
- [23] R. Scheps and J. F. Myers, Dual-wavelength coupled-cavity ti:sapphire laser with active mirror for enhanced red operation and efficient intracavity sum frequency generation at 459 nm, *IEEE Journal of Quantum Electronics* **30**, 1050 (1994).
- [24] Y. Lü, X. Zhang, X. Fu, J. Xia, T. Zheng, and J. Chen, Diode-pumped nd:LuVO<sub>4</sub> and nd:YAG

- crystals yellow laser at 594 nm based on intracavity sum-frequency generation, *Laser Physics Letters* **7**, 634 (2010).
- [25] K. Fradkin, A. Arie, A. Skliar, and G. Rosenman, Tunable midinfrared source by difference frequency generation in bulk periodically poled ktiopo4, *Applied Physics Letters* **74**, 914 (1999), <https://doi.org/10.1063/1.123408>.
- [26] Y. Yamaguchi, R. Hida, T. Suzuki, F. Isa, K. Yoshikiyo, L. Fujii, H. Nemoto, and F. Kannari, Shaping and amplification of wavelength-tunable mid-infrared femtosecond pulses generated by intra-pulse difference-frequency mixing with spectral focusing, *J. Opt. Soc. Am. B* **35**, C1 (2018).
- [27] P. Canarelli, Z. Benko, R. Curl, and F. K. Tittel, Continuous-wave infrared laser spectrometer based on difference frequency generation in aggas2 for high-resolution spectroscopy, *J. Opt. Soc. Am. B* **9**, 197 (1992).
- [28] M. A. Belkin, F. Capasso, F. Xie, A. Belyanin, M. Fischer, A. Wittmann, and J. Faist, Room temperature terahertz quantum cascade laser source based on intracavity difference-frequency generation, *Applied Physics Letters* **92**, 201101 (2008), <https://doi.org/10.1063/1.2919051>.
- [29] K. Vijayraghavan, R. W. Adams, A. Vizbaras, M. Jang, C. Grasse, G. Boehm, M. C. Amann, and M. A. Belkin, Terahertz sources based on Čerenkov difference-frequency generation in quantum cascade lasers, *Applied Physics Letters* **100**, 251104 (2012), <https://doi.org/10.1063/1.4729042>.
- [30] G. Bachelier, I. Russier-Antoine, E. Benichou, C. Jonin, and P.-F. Brevet, Multipolar second-harmonic generation in noble metal nanoparticles, *J. Opt. Soc. Am. B* **25**, 955 (2008).
- [31] R. Zhou, H. Lu, X. Liu, Y. Gong, and D. Mao, Second-harmonic generation from a periodic array of noncentrosymmetric nanoholes, *J. Opt. Soc. Am. B* **27**, 2405 (2010).
- [32] F. D. Luca and C. Cirací, Difference-frequency generation in plasmonic nanostructures: a parameter-free hydrodynamic description, *J. Opt. Soc. Am. B* **36**, 1979 (2019).
- [33] M. Fang, Z. Huang, W. E. I. Sha, and X. Wu, Maxwell–hydrodynamic model for simulating nonlinear terahertz generation from plasmonic metasurfaces, *IEEE Journal on Multiscale and Multiphysics Computational Techniques* **2**, 194 (2017).
- [34] B. S. Mendoza and W. L. Mochán, Exactly solvable model of surface second-harmonic generation, *Phys. Rev. B* **53**, 4999 (1996).
- [35] J. A. Maytorena, B. S. Mendoza, and W. L. Mochán, Theory of surface sum frequency gener-

- ation spectroscopy, *Phys. Rev. B* **57**, 2569 (1998).
- [36] J. Rudnick and E. A. Stern, Second-harmonic radiation from metal surfaces, *Phys. Rev. B* **4**, 4274 (1971).
- [37] J. Recamier, W. L. Mochan, and J. A. Maytorena, Exact nonlinear response of a harmonic oscillator, in *5th Iberoamerican Meeting on Optics and 8th Latin American Meeting on Optics, Lasers, and Their Applications*, Vol. 5622, edited by A. M. O. and J. L. Paz, International Society for Optics and Photonics (SPIE, 2004) pp. 513 – 517.
- [38] J. D. Jackson, *Classical electrodynamics; 2nd ed.* (Wiley, New York, NY, 1975).
- [39] V. Agranovich and Y. Gartstein, Electrodynamics of metamaterials and the landau–lifshitz approach to the magnetic permeability, *Metamaterials* **3**, 1 (2009).
- [40] N. Ashcroft and N. Mermin, *Solid State Physics* (Saunders College, Philadelphia, 1976).
- [41] A. V. Petukhov, V. L. Brudny, W. L. Mochán, J. A. Maytorena, B. S. Mendoza, and T. Rasing, Energy conservation and the manley-rowe relations in surface nonlinear-optical spectroscopy, *Phys. Rev. Lett.* **81**, 566 (1998).
- [42] Supplementary video: An animation illustrating the evolution of the nonlinear electromagnetic radiation pattern for different input frequencies. the radiation pattern are plotted superimposed on the frequency space map which shows the region of the largest contributing parameter to the nonlinear efficiency. a square point moving across the map denotes the values of the two input frequencies to which the pattern corresponds.